

Proton spin structure and generalized polarizabilities in the strong quantum chromodynamics regime

Received: 23 April 2022

Accepted: 2 September 2022

Published online: 13 October 2022



A list of authors and their affiliations appears at the end of the paper

The strong interaction is not well understood at low energies or for interactions with low momentum transfer. Chiral perturbation theory gives testable predictions for the nucleonic generalized polarizabilities, which are fundamental quantities describing the nucleon's response to an external field. We report a measurement of the proton's generalized spin polarizabilities extracted with a polarized electron beam and a polarized solid ammonia target in the region where chiral perturbation theory is expected to be valid. The investigated structure function g_2 characterizes the internal spin structure of the proton. From its moments, we extract the longitudinal–transverse spin polarizability δ_{LT} and twist-3 matrix element and polarizability \overline{d}_2 . Our results provide discriminating power between existing chiral perturbation theory calculations and will help provide a better understanding of this strong quantum chromodynamics regime.

The proton accounts for the vast majority of ordinary matter in the Universe, but how its fundamental properties such as mass and spin arise from the interactions of its constituents remains an open question. The proton's sub-structure is well understood in the high-energy short-distance region of asymptotic freedom¹. Conversely, in the low-energy regime where the quantum chromodynamics (QCD) coupling becomes truly strong, quark–quark and quark–gluon correlations invalidate the simple picture of the parton model. Unresolved questions about the structure of the proton can be probed with spin-polarized electron–proton scattering, but this region carries a number of experimental challenges that make data scarce. These challenges are especially difficult at low energy for transversely polarized protons, as a low-energy incident electron beam will suffer severe bending in the transverse target magnetic field, introducing a number of systematic issues.

The nucleons are not yet well understood in this regime. For example, neutron data² revealed a large discrepancy between moments of the spin structure functions and early calculations of chiral perturbation theory (χ PT). This discrepancy became known as the ‘ δ_{LT} puzzle’ and stimulated a rigorous new generation of theoretical efforts and low- Q^2 experiments such as the present measurement. Though some light has been shed on the initial disagreement, the newest neutron data³ still show a large deviation from χ PT, making it very important to

examine if similar issues exist for the proton. Several recently published experiments^{3,4} have probed the low- and medium-energy regions of the spin structure function g_1^p and the medium-energy region of the spin structure function g_2^p . Our experiment expands on those results with low-energy measurements of g_2^p and its associated moments.

Sum rules and moments of the nucleon spin structure functions allow for a direct comparison between experiment and theory. In recent years, the Bjorken sum rule⁵ at large Q^2 and the Gerasimov–Drell–Hearn (GDH) sum rule⁶ at $Q^2 = 0$ have been extensively investigated^{7–11}. Less well studied for the proton is another class of sum rules addressing the spin polarizabilities^{12,13}. Spin polarizabilities are fundamental properties of the nucleons, making their measurement and comparison to theory of great interest. Polarizabilities, in general, describe the proton's response to an external field. The electric and magnetic polarizabilities are relatively well measured for the proton, but less well understood are the spin and colour polarizabilities. Spin polarizabilities describe a spin-dependent response of the nucleon to an electromagnetic field, whereas colour polarizabilities contain information on how the nucleon's spin affects the colour electric and magnetic fields on average^{14,15}. Of particular interest is the spin polarizability δ_{LT} and the higher moment \overline{d}_2 related to the colour polarizabilities at large Q^2 .

✉ e-mail: karl.slifer@unh.edu

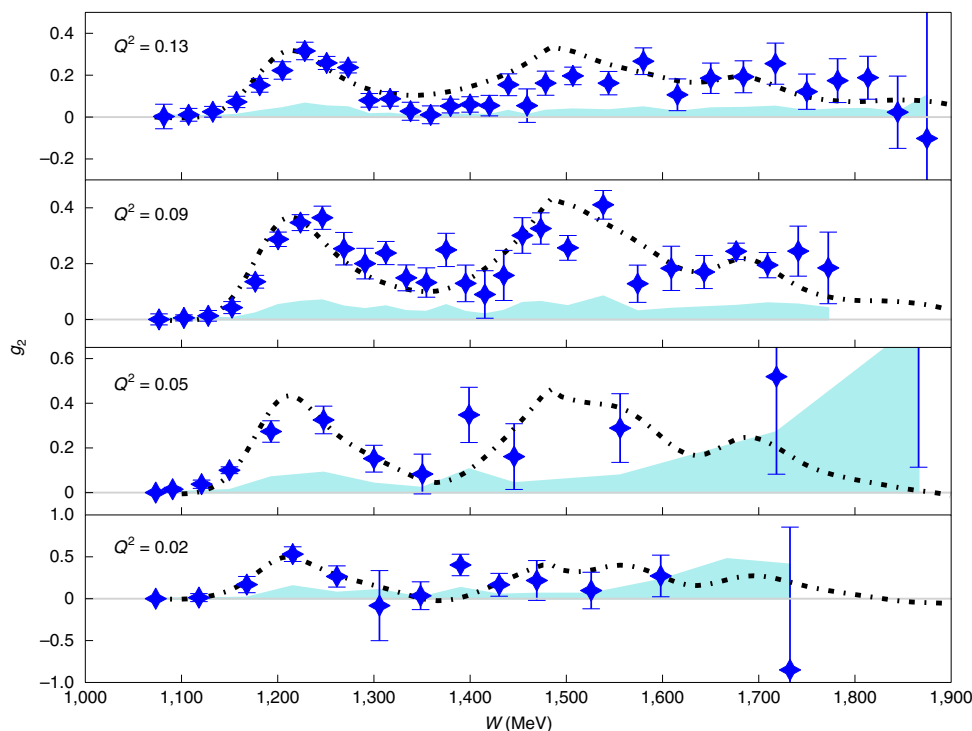


Fig. 1 | Proton spin structure function g_2 as a function of invariant mass W . Each panel is adjusted to a constant momentum transfer Q^2 (value in the upper-left corner); this Q^2 value is presented in units of GeV^2 . The error bars are statistical and are the result of propagating the standard deviation of the raw measured counts through the final analysis. The shaded region represents the

systematic uncertainty, which is dominated by the unpolarized model systematic and dilution factor, as discussed in the main text. The black dashed line represents the phenomenological Hall B model^{34,35}. The grey line indicates zero to more easily distinguish sign changes in the data.

The sum rules used to obtain these moments are based on unsubtracted dispersion relations, which use the optical theorem to relate moments of the spin structure functions to real or virtual Compton amplitudes¹⁶. The doubly virtual Compton-scattering dispersion relations are used to form a low-energy expansion of the spin-flip Compton amplitudes f_{TT} and f_{LT} (ref. ¹⁷), giving rise to a number of spin structure function moments. The next-to-leading order term of the f_{LT} low-energy expansion contains the following generalized longitudinal-transverse spin polarizability:

$$\delta_{\text{LT}}(Q^2) = \frac{16\alpha M^2}{Q^6} \int_0^{x_0} x^2 (g_1(x, Q^2) + g_2(x, Q^2)) dx. \quad (1)$$

Here Q^2 is the four-momentum transfer, α is the fine-structure constant, M represents the proton mass and x_0 represents the Bjorken x value associated with the pion production threshold at an invariant mass (defined as $W^2 = M^2 + 2M\nu - Q^2$) for $W = 1,073.2$ MeV. This limit ensures that the elastic response is excluded from the integral as is required for pure polarizability¹⁵.

A measurement of the generalized longitudinal-transverse polarizability is considered a benchmark test of χ PT because it is a fundamental nucleon observable and was initially expected to be insensitive to contributions from virtual π - Δ intermediate states^{18,19}. The actual contribution of these states has ultimately proved to be more complicated. The χ PT predictions for δ_{LT} at leading order and next-to-leading order are, in principle, parameter-free predictions, the accuracy of which is only determined by the convergence properties of chiral expansion. Precise comparisons of this quantity between data and theory are, therefore, extremely valuable to test χ PT and other low-energy theories.

Also of interest is the \overline{d}_2 spin polarizability, a higher moment identified at high Q^2 with the twist-3 matrix element d_2 (ref. ¹⁴). We can access a truncated moment of this quantity through a sum rule:

Table 1 | Kinematics of the E08-027 experiment

E_0 (MeV)	E' (MeV)	Field (T)	Configuration	θ_e (°)	Q^2 (GeV^2)
1,711	577–1,691	2.5	perp	5–8	0.021
2,254	541–2,228	2.5	perp	6–9	0.045
2,254	991–2,228	5.0	par	6	0.045
2,254	919–2,228	5.0	perp	7–13	0.086
3,350	1,945–3,000	5.0	perp	6–8	0.130

E_0 represents the energy of the incident electron beam for each setting. The scattering angles θ_e at the perpendicular target-field configurations represent the approximate range, influenced by the target field. Smaller scattering angles correspond to larger values of scattered electron energy E' . The reported momentum transfer Q^2 is the extrapolated constant Q^2 value. The table rows correspond to different beam energies at which the experiment was run at, whereas the columns show the associated kinematic variables for each setting. All the settings with the configuration ‘perp’ were run with the target field perpendicular to the electron beam, whereas the one with the configuration ‘par’ was run with a target field parallel to the electron beam.

$$\overline{d}_2(Q^2) = \int_0^{x_0} x^2 (2g_1(x, Q^2) + 3g_2(x, Q^2)) dx. \quad (2)$$

At high Q^2 , this moment describes the ‘colour Lorentz force’ and gives us information on the colour polarizabilities discussed above. Consequently, \overline{d}_2 helps to describe how the colour electric and magnetic fields interact with the nucleon spin¹⁴. In this regime, \overline{d}_2 becomes a twist-3 quantity and thus quantifies the quark–gluon correlations of the nucleon²⁰. At low Q^2 , the partonic description of \overline{d}_2 fails, but it remains pure polarizability that contains information on the nucleon’s bulk properties at the hadronic level^{15,21}. The moment vanishes for $Q^2 = 0$ and $Q^2 = \infty$, but must also smoothly transition through these very different regimes, with phenomenological models suggesting a

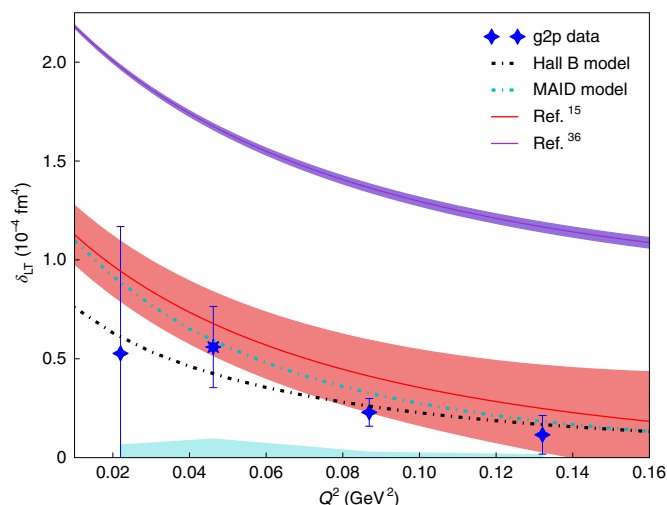


Fig. 2 | Longitudinal-transverse spin polarizability δ_{LT} (10^{-4} fm^4) for the proton. The data are given as a function of momentum transfer Q^2 . The data from this experiment are presented with blue stars, with the eight-pointed marker near $Q^2 = 0.05 \text{ GeV}^2$ including both g_1 and g_2 from the E08-027 data, and the other three points making use of the CLAS model³⁵ for the g_1 part of the integral. The error bars indicate the statistical error, which comes from the standard deviation of the raw counts propagated through the final analysis. The cyan-shaded region represents the systematic uncertainty, which is dominated by the unpolarized model systematic and dilution factor, as discussed in the main text. The red band represents the upper and lower limits of the calculation in ref. 15, and the purple band represents the limits of the calculation in ref. 36. Details on the error of these calculations is available in the corresponding publications. The black dashed line indicates the phenomenological CLAS Hall B model³⁵, whereas the cyan dashed line indicates the MAID model³³.

maximum in the transition region around 1 GeV^2 (ref. 22). A measurement of d_2 over a broad region will help to understand the transition between the partonic and hadronic descriptions of the nucleon²¹, but data for this observable have proven to be difficult to obtain.

In this Article, we present the measurement of the proton spin structure function g_2 for a range of Q^2 from 0.02 to 0.13 GeV^2 . We extract the polarizabilities δ_{LT} and d_2 and compare our results with the leading predictions of χ PT.

The E08-027 (g2p) experiment²³ was performed in Hall A at the Thomas Jefferson National Accelerator Facility. We performed an inclusive measurement at the forward angles of the proton spin-dependent cross sections. A longitudinally polarized electron beam was scattered off a longitudinally or transversely polarized solid ammonia target. Data were collected at three different beam energies and two different target field strengths. The transverse field of the transversely polarized ammonia target sufficiently influenced the scattered electron trajectory to yield two separate Q^2 values at a single beam energy for different target magnetic-field strengths. In total, the results cover five transverse-field kinematic settings and one longitudinal-field setting (Table 1). The measurements covered values of invariant mass from the nuclear elastic peak through the nucleon resonance region, but only the results above the pion production threshold ($W = 1,073.2 \text{ MeV}$) are discussed in this Article.

We extracted the spin structure functions from a calculation of the polarized cross-section differences $\Delta\sigma_{\parallel} = \frac{d^2\sigma}{d\Omega dE'}(\uparrow\uparrow - \uparrow\downarrow)$ and $\Delta\sigma_{\perp} = \frac{d^2\sigma}{d\Omega dE'}(\downarrow\Rightarrow - \uparrow\Rightarrow)$ and these two polarized cross-section differences correspond to the target proton spin parallel and perpendicular to the incoming electron spin, respectively. These cross-section differences were formed by combining the measured asymmetry with a model unpolarized cross section. The slightly differing kinematics, influenced by the strong target magnetic field, did not

permit the combination of datasets at the polarized cross-section difference level for the setting where we have both longitudinal and transverse data; therefore, the structure functions were formed according to

$$g_1(x, Q^2) = K_1 \left[\Delta\sigma_{\parallel} \left(1 + \frac{1}{K_2} \tan \frac{\theta}{2} \right) \right] + \frac{2g_2 \tan \frac{\theta}{2}}{K_2 y}, \quad (3)$$

$$g_2(x, Q^2) = \frac{K_1 y}{2} \left[\Delta\sigma_{\perp} \left(K_2 + \tan \frac{\theta}{2} \right) \right] - \frac{g_1 y}{2}, \quad (4)$$

where the kinematic terms K_1 and K_2 are defined as

$$K_1 = \frac{MQ^2}{4\alpha} \frac{y}{(1-y)(2-y)}, \quad (5)$$

$$K_2 = \frac{1 + (1-y) \cos \theta}{(1-y) \sin \theta}, \quad (6)$$

and θ is the angle of the scattered electron, $y = v/E$ and $v = E' - E$. A model²⁴ based on the CLAS Hall B data was used as the g_1 input for the extraction of g_2 , except in the $Q^2 = 0.05 \text{ GeV}^2$ setting where the measured values of $\Delta\sigma_{\parallel}$ and $\Delta\sigma_{\perp}$ were used to solve the above for g_1 and g_2 , respectively. Details on the extraction of the polarized cross-section differences and asymmetries used to form them can be found in the Methods section.

The experimental cross section, calculated only for the longitudinal setting, was formed by normalizing the detected electron counts by target density and thickness (ρ), spectrometer acceptance (V_{acc}), detector efficiencies (ϵ_{det}), lifetime (LT) and accumulated charge (q/e):

$$\sigma_0 = \frac{d^2\sigma}{d\Omega dE'} = \frac{N_{\text{det}}}{q/e \times \rho \times \text{LT} \times \epsilon_{\text{det}} \times V_{\text{acc}}}. \quad (7)$$

The spectrometer acceptance is defined with solid angle Ω and scattered electron energy E' and was determined using a Monte Carlo simulation²⁵. The same dilution factor in the asymmetry was applied to the cross section to obtain a pure proton result; this dilution factor corrects the contributions from other materials and is fully explained in the Methods section. Large systematics in the transverse cross sections made it preferable to form the polarized cross-section differences using the asymmetries from the g2p data and an unpolarized cross section from the Bosted-Christy model²⁶. The longitudinal cross section was used to determine how well the model agreed with the g2p data and obtain an associated systematic error. From this comparison, it was determined that the structure of the model matched our data very well, but needed to be scaled by a factor of ≈ 1.15 . This scaling factor is perhaps not surprising due to the small amount of existing low- Q^2 proton data available to constrain the model and is in any case consistent within the error bars with the E61 data²⁷ that were originally used to create the Bosted-Christy model. This scaling factor is trusted to within the 9% relative uncertainty of our measured cross section. An additional small uncertainty associated with structure differences between our data and the model brings the uncertainty of this method to around 10%. However, the impact of this scaling factor on the higher moments is suppressed. We have calculated it to be less than 6% relative uncertainty, which contributes to the total uncertainty at the same order as the dilution factor.

The uncertainty in the dilution factor is a product of uncertainty propagated from the calculation of the packing fraction and uncertainty associated with acceptance effects; this systematic value averaged between 6% and 8%. The uncertainty in the reconstructed electron-scattering angle is a product of the beam position monitor and spectrometer optics uncertainties; this angle uncertainty is

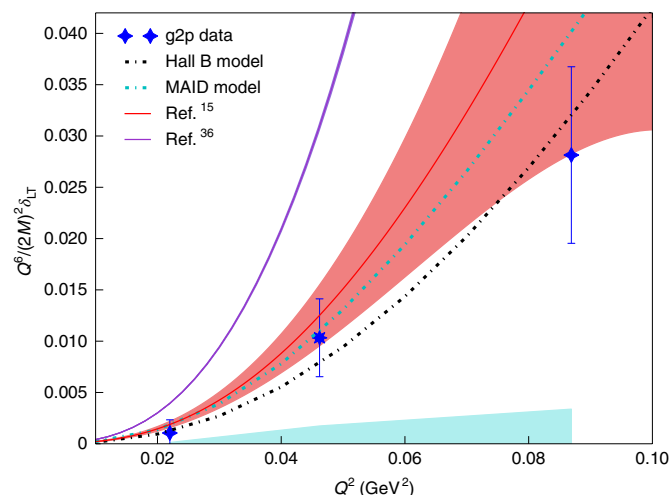


Fig. 3 | Unitless scaling of the longitudinal-transverse spin polarizability $\frac{Q^6}{(2M)^2} \delta_{LT}$ for the proton. Data are given as a function of momentum transfer Q^2 .

The data from this experiment are presented with blue stars, with the eight-pointed marker near $Q^2 = 0.05 \text{ GeV}^2$ including both g_1 and g_2 from the E08-027 data, and the other three points making use of the CLAS model³⁵ for the g_1 part of the integral. The error bars indicate the statistical error, which comes from the standard deviation of the raw counts propagated through the final analysis. The cyan-shaded region represents the systematic uncertainty, which is dominated by the unpolarized model systematic and dilution factor, as discussed in the main text. The red band represents the upper and lower limits of the calculation in ref. ¹⁵, and the purple band represents the limits of the calculation in ref. ³⁶. Details on the error of these calculations is available in the corresponding publications. The black dashed line indicates the phenomenological CLAS Hall B model³⁵, whereas the cyan dashed line indicates the MAID model³³.

approximately 2% and when it propagates through the Mott cross section at forward angles, a systematic uncertainty of 5% is found. The beam and target polarizations contribute an uncertainty of around 5%, and the radiative corrections and elastic-tail subtraction contribute around 3% each. The uncertainty associated with the g_1/g_2 input to the polarized cross-section differences was 2% or less. The contribution of the out-of-plane angle, adjustment to constant Q^2 , charge normalization and detector efficiencies were found to contribute 1% uncertainty or less to the total systematic. Adding the above errors in quadrature produces an approximately 14% systematic uncertainty in each kinematic setting for the structure function, which is slightly reduced to 12% in the moments by kinematic weighting. This systematic breakdown is shown in detail in Extended Data Table 1.

Radiative corrections were applied using a combination of the Mo and Tsai (external corrections)²⁸ and POLRAD (internal corrections) formalisms^{29,30}. The polarized elastic-tail contributions were calculated using the Ye and Arrington elastic form-factor parametrization³¹. Inelastic corrections were calculated using an iterative unfolding procedure. All the unpolarized corrections were calculated under the energy-peaking approximation³². A combination of g2p data and polarized model inputs (MAID and CLAS³³⁻³⁵) was incorporated into the process to improve the systematic uncertainty. Extrapolations in the iterative procedure were carried out at lines of constant W where the input spectra exhibited the same angular dependence as the unfolded cross section²³.

Our results for the spin structure functions evaluated at constant Q^2 are shown in Fig. 1 as a function of invariant mass W . Blue stars are g_2 results from our perpendicular polarized cross-section differences. For the moments shown in this Article, data that include a model for the g_1 part are represented with these four-pointed markers. Data that instead include the E08-027 g_1 data (not displayed here) are represented with

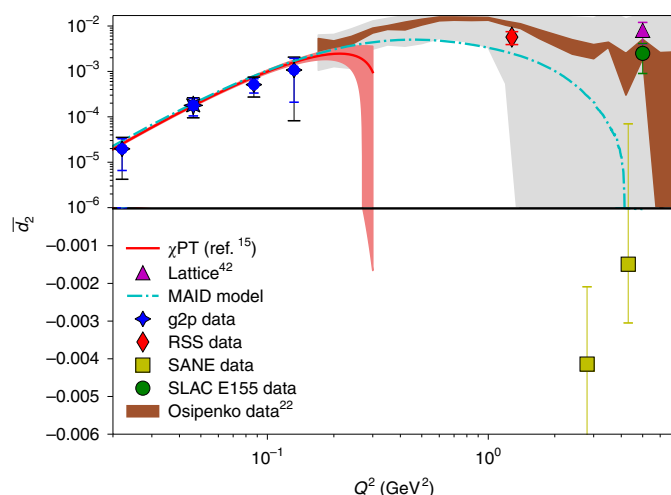


Fig. 4 | Higher moment \bar{d}_2 for the proton. Data are given as a function of momentum transfer Q^2 . The data from this experiment are presented with blue stars, with the eight-pointed marker near $Q^2 = 0.05 \text{ GeV}^2$ including both g_1 and g_2 from the E08-027 data, and the other three points making use of the CLAS model³⁵ for the g_1 part of the integral. The inner error bars indicate the statistical error, which comes from the standard deviation of the raw counts propagated through the final analysis. The outer black error bars represent the systematic uncertainty, which is dominated by the unpolarized model systematic and dilution factor, as discussed in the main text. The red band represents the upper and lower limits of the calculation in ref. ¹⁵ and details on the error of this calculation are available in the corresponding publication. The cyan dashed line indicates the phenomenological MAID model³³. The moment is compared with the existing data of the RSS experiment (red diamond)⁴⁰, SANE experiment (yellow square)³⁹ and SLAC E155 experiment (green circle)⁴¹. A lattice QCD calculation at 5 GeV^2 (ref. ⁴²) is indicated by a magenta triangle. The brown band is the Osipenko model and the grey region is the associated error band, details of which are available in the associated publications²². The region above zero is shown on a log scale on the y axis to clearly show the comparison with the model, whereas the negative half of the plot is shown on a linear scale to allow the proper inclusion of the SANE³⁹ data. The black line just below 10^{-6} indicates a \bar{d}_2 value of zero.

eight-pointed markers (Figs. 2, 3 and 4, $Q^2 = 0.04 \text{ GeV}^2$). In all the figures, the error bars are the statistical uncertainty, and the blue-shaded region beneath the data is the systematic uncertainty. Numerical values for the structure functions shown are found in the Source data.

The adjustment to a constant momentum transfer assumes the Q^2 dependence of the CLAS model^{34,35}, although the MAID model predicted a similar evolution. For all our spectra, the correction was small compared with the statistical uncertainty of the spin structure function. The method is described in detail elsewhere²³ and contributed less than 1% systematic uncertainty.

These constant- Q^2 structure functions were used to form the moments defined in equations (1) and (2). Our measured spin structure function data extends down to at least $x = 0.05$ for all Q^2 . This combined with x^2 weighting of the integrals ensures that the moments are largely insensitive to any unmeasured contribution at lower x . The numerical results for the moments displayed here are available in Table 2.

Our results for the longitudinal-transverse spin polarizability (δ_{LT} ; Fig. 2) represent a high-precision experimental determination of a previously unmeasured quantity for the proton. Figure 3 is scaled from the same data to form a unitless quantity, which emphasizes the lowest- Q^2 data¹². Comparisons were made to relativistic baryon- χ PT calculations^{15,36} and are represented by the red and purple bands. The solid lines represent the central values, whereas the shaded bands represent the calculation's uncertainty. Within our uncertainties, we show general agreement with the calculation from ref. ¹⁵ and disagreement with the calculation from ref. ³⁶.

Table 2 | Summary of the E08-027 moment results

	Q^2 (GeV ²)	Measured	Statistical	Systematic
δ_{LT} (10 ⁻⁴ fm ⁴)	0.021	0.534	0.641	0.064
	0.045	0.828	0.187	0.138
	0.086	0.227	0.070	0.027
	0.130	0.111	0.097	0.013
$\overline{d_2}$	0.021	1.97e-5	1.31e-5	2.36e-6
	0.045	5.72e-5	1.75e-5	9.55e-6
	0.086	5.11e-4	8.84e-5	6.13e-5
	0.130	1.07e-3	4.32e-4	1.28e-4

The first column indicates what momentum transfer Q^2 each result is associated with, whereas the other three columns (in order) indicate the measured central value, statistical uncertainty and systematic uncertainty, respectively. The first four rows present the results of the δ_{LT} polarizability and the next four rows give the results of the $\overline{d_2}$ moment.

One known difference between the two calculations rises from the inclusion of the $\Delta(1,232)$ resonance through a perturbative expansion. Ref. ³⁶ adheres to an ϵ expansion scheme, where the mass difference between the Δ resonance and proton (Δ) is assumed to be of similar scale to the pion mass m_π , allowing them to be expanded to the same order. Ref. ¹⁵ uses a δ -power counting scheme, which assumes that the ratio of these parameters $\frac{m_\pi}{\Delta}$ is similar to the ratio of Δ and nucleon mass, that is, $\frac{\Delta}{M_p}$ (ref. ³⁷). It is interesting to note that the Q^2 dependence

of the calculations is similar, but the normalizations appear to substantially differ (Fig. 2). As discussed elsewhere¹⁵, such a difference at $Q^2 = 0$ could result from their enforcement of ‘consistent’ couplings to the delta field, as opposed to the discussions in ref. ³⁶ where this consistency is not enforced; also, the results from that study include only the leading-order predictions. A recent analysis³⁸ indicates that higher-order corrections are expected to be large. A comparison that accounts for these additional corrections is necessary to completely understand the underlying differences between the two theoretical approaches.

Our results for the higher moment $\overline{d_2}$ are shown in Fig. 4. These data show good agreement with the MAID model³³ and the calculation in ref. ¹⁵. The brown-shaded (and grey-shaded) regions are a result of using the Osipenko model²² to generate a $\overline{d_2}$ prediction. The spin asymmetries of the nucleon (SANE)³⁹ data at high Q^2 indicates the intriguing possibility of a zero crossing at large Q^2 , whereas our data are consistent with the positive sign of the RSS⁴⁰ and SLAC⁴¹ data, as well as a lattice QCD⁴² calculation. On this plot, the region above zero is shown on a log scale to make the structure of our data visible, and the region below zero is shown on a linear scale to allow the inclusion of the SANE data. Our data show the expected trend towards zero at the real photon point. Confirmation of the maximum predicted by the phenomenological models around 1 GeV² will require further measurements of g_2 in this region.

These polarizabilities provide insights into the non-perturbative regime of the proton. The $\overline{d_2}$ results show good agreement with phenomenological models and the Alarcón¹⁵ χ PT calculation and suggest that a new medium- Q^2 measurement is important to understand the transition region. Our results allow for unambiguous discrimination between two state-of-the-art χ PT calculations for the longitudinal-transverse spin polarizability, supporting the calculation in ref. ¹⁵. In contrast to the original δ_{LT} puzzle, the proton calculations show better agreement with the data than originally observed for the neutron, although our data clearly favour one approach. These data represent a benchmark for a high-precision discrimination of the theoretical calculations in the strong QCD domain.

Online content

Any methods, additional references, Nature Research reporting summaries, source data, extended data, supplementary information, acknowledgements, peer review information; details of author contributions and competing interests; and statements of data and code availability are available at <https://doi.org/10.1038/s41567-022-01781-y>.

References

1. Feynman, R. P. Very high-energy collisions of hadrons. *Phys. Rev. Lett.* **23**, 1415–1417 (1969).
2. Amarian, M. et al. Measurement of the generalized forward spin polarizabilities of the neutron. *Phys. Rev. Lett.* **93**, 152301 (2004).
3. Sulkosky, V. et al. Measurement of the generalized spin polarizabilities of the neutron in the low- Q^2 region. *Nat. Phys.* **17**, 687–692 (2021).
4. Zheng, X. et al. Measurement of the proton spin structure at long distances. *Nat. Phys.* **17**, 736–741 (2021).
5. Bjorken, J. D. Asymptotic sum rules at infinite momentum. *Phys. Rev.* **179**, 1547–1553 (1969).
6. Drell, S. D. & Hearn, A. C. Exact sum rule for nucleon magnetic moments. *Phys. Rev. Lett.* **16**, 908–911 (1966).
7. Alekseev, M. G. et al. The spin-dependent structure function of the proton g_1^p and a test of the Bjorken sum rule. *Phys. Lett. B* **690**, 466–472 (2010).
8. Deur, A. et al. Experimental determination of the evolution of the Bjorken integral at low Q^2 . *Phys. Rev. Lett.* **93**, 212001 (2004).
9. Drechsel, D., Kamalov, S. S. & Tiator, L. Gerasimov-Drell-Hearn sum rule and related integrals. *Phys. Rev. D* **63**, 114010 (2001).
10. Deur, A. et al. Experimental study of isovector spin sum rules. *Phys. Rev. D* **78**, 032001 (2008).
11. Adolph, C. et al. Final COMPASS results on the deuteron spin-dependent structure function g_1^d and the Bjorken sum rule. *Phys. Lett. B* **769**, 34–41 (2017).
12. Drechsel, D., Pasquini, B. & Vanderhaeghen, M. Dispersion relations in real and virtual Compton scattering. *Phys. Rep.* **378**, 99–205 (2003).
13. Deur, A., Brodsky, S. J. & de Téramond, G. F. The spin structure of the nucleon. *Rep. Prog. Phys.* **82**, 076201 (2019).
14. Meziani, Z. E. et al. Higher twists and color polarizabilities in the neutron. *Phys. Lett. B* **613**, 148–153 (2005).
15. Alarcón, J. M., Hagelstein, F., Lensky, V. & Pascalutsa, V. Forward doubly-virtual Compton scattering off the nucleon in chiral perturbation theory. II. Spin polarizabilities and moments of polarized structure functions. *Phys. Rev. D* **102**, 114026 (2020).
16. Chen, J.-P. Moments of spin structure functions: sum rules and polarizabilities. *Int. J. Mod. Phys. E* **19**, 1893–1921 (2012).
17. Drechsel, D. Spin sum rules and polarizabilities. *AIP Conf. Proc.* **1155**, 3 (2009).
18. Bernard, V., Hemmert, T. R. & Meissner, U.-G. Novel analysis of chiral loop effects in the generalized Gerasimov-Drell-Hearn sum rule. *Phys. Lett. B* **545**, 105–111 (2002).
19. Kao, C.-W., Spitzenberg, T. & Vanderhaeghen, M. Burkhardt-Cottingham sum rule and forward spin polarizabilities in heavy baryon chiral perturbation theory. *Phys. Rev. D* **67**, 016001 (2003).
20. Burkardt, M. The g_2 structure function. *AIP Conf. Proc.* **1155**, 26–34 (2009).
21. Kao, C.-W., Drechsel, D., Kamalov, S. & Vanderhaeghen, M. Higher moments of nucleon spin structure functions in heavy baryon chiral perturbation theory and in a resonance model. *Phys. Rev. D* **69**, 056004 (2004).
22. Osipenko, M. et al. Global analysis of data on the proton structure function g_1 and extraction of its moments. *Phys. Rev. D* **71**, 054007 (2005).

23. Zielinski, R. *The g_2^p Experiment: A Measurement of the Proton's Spin Structure Functions*. PhD thesis, Univ. of New Hampshire (2017).
 24. CLAS Physics Database. <http://clas.sinp.msu.ru/cgi-bin/jlab/db.cgi/> (2019).
 25. Gu, C. *The Spin Structure of the Proton at Low Q^2 : A Measurement of the Structure Function g_2^p* . PhD thesis, Univ. of Virginia (2016).
 26. Christy, M. E. & Bosted, P. E. Empirical fit to precision inclusive electron-proton cross sections in the resonance region. *Phys. Rev. C* **81**, 055213 (2010).
 27. Collaboration, H. C. Hall C Resonance Data Archive; <https://hallcweb.jlab.org/resdata/database/>
 28. Mo, L. W. & Tsai, Y. S. Radiative corrections to elastic and inelastic ep and up scattering. *Rev. Mod. Phys.* **41**, 205–235 (1969).
 29. Akushevich, I., Ilyichev, A., Shumeiko, N., Soroko, A. & Tolkachev, A. POLARD 2.0 FORTRAN code for the radiative corrections calculation to deep inelastic scattering of polarized particles. *Comput. Phys. Commun.* **104**, 201–244 (1997).
 30. Afanasev, A. V., Akushevich, I., Ilyichev, A. & Merenkov, N. P. QED radiative corrections to asymmetries of elastic ep scattering in hadronic variables. *Phys. Lett. B* **514**, 269–278 (2001).
 31. Ye, Z., Arrington, J., Hill, R. J. & Lee, G. Proton and neutron electromagnetic form factors and uncertainties. *Phys. Lett. B* **777**, 8–15 (2018).
 32. Stein, S. et al. Electron scattering at 4 degrees with energies of 4.5–20 GeV. *Phys. Rev. D* **12**, 1884 (1975).
 33. Drechsel, D., Kamalov, S. S. & Tiator, L. Unitary isobar model—MAID2007. *Eur. Phys. J. A* **34**, 69–97 (2007).
 34. Guler, N. *Measurement of Longitudinal Double Spin Asymmetries and Spin Structure Functions of the Deuteron in the CLAS EG1b Experiment*. Tech. Rep. CLAS EG1b Collaboration (2012).
 35. Fersch, R. et al. Determination of the proton spin structure functions for $0.05 < Q^2 < 5 \text{ GeV}^2$ using CLAS. *Phys. Rev. C* **96**, 065208 (2017).
 36. Bernard, V., Epelbaum, E., Krebs, H. & Meissner, U.-G. New insights into the spin structure of the nucleon. *Phys. Rev. D* **87**, 054032 (2013).
 37. Pascalutsa, V. & Phillips, D. R. Model-independent effects of Δ excitation in nucleon polarizabilities. *Phys. Rev. C* **68**, 055205 (2003).
 38. Thürmann, M., Epelbaum, E., Gasparyan, A. M. & Krebs, H. Nucleon polarizabilities in covariant baryon chiral perturbation theory with explicit Δ degrees of freedom. *Phys. Rev. C* **103**, 035201 (2021).
 39. Armstrong, W. et al. Revealing color forces with transverse polarized electron scattering. *Phys. Rev. Lett.* **122**, 022002 (2019).
 40. Wesselmann, F. R. et al. Proton spin structure in the resonance region. *Phys. Rev. Lett.* **98**, 132003 (2007).
 41. Anthony, P. L. et al. Precision measurement of the proton and deuteron spin structure functions g_2 and asymmetries A_2 . *Phys. Lett. B* **553**, 18–24 (2003).
 42. Gockeler, M. et al. A lattice calculation of the nucleon's spin dependent structure function g_2 revisited. *Phys. Rev. D* **63**, 074506 (2001).
- Publisher's note** Springer Nature remains neutral with regard to jurisdictional claims in published maps and institutional affiliations.
- Springer Nature or its licensor holds exclusive rights to this article under a publishing agreement with the author(s) or other rightsholder(s); author self-archiving of the accepted manuscript version of this article is solely governed by the terms of such publishing agreement and applicable law.
- © The Author(s), under exclusive licence to Springer Nature Limited 2022

D. Ruth¹, **R. Zielinski**¹, **C. Gu**², **M. Allada (Cummings)**³, **T. Badman**¹, **M. Huang**⁴, **J. Liu**², **P. Zhu**⁵, **K. Allada**⁶, **J. Zhang**⁷, **A. Camsonne**⁷, **J.-P. Chen**⁷, **K. Slifer**¹✉, **K. Aniol**⁸, **J. Annand**⁹, **J. Arrington**^{10,11}, **T. Averett**¹², **H. Baghdasaryan**², **V. Bellini**¹², **W. Boeglin**¹³, **J. Brock**⁷, **C. Carlin**⁷, **C. Chen**¹⁴, **E. Cisbani**¹⁵, **D. Crabb**², **A. Daniel**², **D. Day**², **R. Duve**², **L. El Fassi**^{16,17}, **M. Friedman**¹⁸, **E. Fuchey**¹⁹, **H. Gao**⁴, **R. Gilman**¹⁶, **S. Glamazdin**²⁰, **P. Gueye**¹⁴, **M. Hafez**^{21,22}, **Y. Han**¹⁴, **O. Hansen**¹⁶, **M. Hashemi Shabestari**², **O. Hen**⁶, **D. Higinbotham**¹⁶, **T. Horn**²³, **S. Iqbal**⁸, **E. Jensen**²⁴, **H. Kang**²⁵, **C. D. Keith**⁷, **A. Kelleher**⁶, **D. Keller**², **H. Khanal**¹³, **I. Korover**²⁶, **G. Kumbartzki**¹⁶, **W. Li**²⁷, **J. Lichtenstadt**²⁶, **R. Lindgren**², **E. Long**¹, **S. Malace**²⁸, **P. Markowitz**¹³, **J. Maxwell**^{1,7}, **D. M. Meekins**¹⁶, **Z. E. Meziani**¹⁹, **C. McLean**¹³, **R. Michaels**⁷, **M. Mihovilovic**^{29,30}, **N. Muangma**⁶, **C. Munoz Camacho**³¹, **J. Musson**⁷, **K. Myers**¹⁶, **Y. Oh**²⁵, **M. Pannunzio Carmignotto**²³, **C. Perdrisat**³, **S. Phillips**¹, **E. Piasetzky**²⁶, **J. Pierce**^{7,32}, **V. Punjabi**³³, **Y. Qiang**⁷, **P. E. Reimer**¹⁰, **Y. Roblin**¹⁶, **G. Ron**¹⁸, **O. Rondon**², **G. Russo**¹², **K. Saenboonruang**², **B. Sawatzky**⁷, **A. Shahinyan**³⁴, **R. Shneor**²⁶, **S. Širca**^{29,30}, **J. Sjoegren**⁹, **P. Solvignon-Slifer**^{1,37}, **N. Sparveris**¹⁹, **V. Sulkosky**⁶, **F. Wesselmann**³⁵, **W. Yan**⁵, **H. Yang**³⁶, **H. Yao**³, **Z. Ye**¹⁶, **M. Yurov**¹⁶, **Y. Zhang**¹⁶, **Y. X. Zhao**⁵ and **X. Zheng**¹²

¹University of New Hampshire, Durham, NH, USA. ²University of Virginia, Charlottesville, VA, USA. ³The College of William and Mary, Williamsburg, VA, USA. ⁴Duke University, Durham, NC, USA. ⁵University of Science and Technology, Hefei, China. ⁶Massachusetts Institute of Technology, Cambridge, MA, USA. ⁷Thomas Jefferson National Accelerator Facility, Newport News, VA, USA. ⁸California State University, Los Angeles, Los Angeles, CA, USA. ⁹Glasgow University, Glasgow, Scotland. ¹⁰Argonne National Laboratory, Argonne, IL, USA. ¹¹Lawrence Berkeley National Laboratory, Berkeley, CA, USA. ¹²Università di Catania, Catania, Italy. ¹³Florida International University, Miami, FL, USA. ¹⁴Hampton University, Hampton, VA, USA. ¹⁵Istituto Nazionale di Fisica Nucleare, Sezione di Roma Tor Vergata, Rome, Italy. ¹⁶Rutgers University, New Brunswick, NJ, USA. ¹⁷Mississippi State University, Mississippi State, Starkville, MS, USA. ¹⁸Hebrew University, Jerusalem, Israel. ¹⁹Temple University, Philadelphia, PA, USA. ²⁰Kharkov Institute of Physics and Technology, Kharkov, Ukraine. ²¹Old Dominion University, Norfolk, VA, USA. ²²Cairo University, Giza, Egypt. ²³Catholic University of America, Washington, DC, USA. ²⁴Christopher Newport University, Newport News, VA, USA. ²⁵Seoul National University, Seoul, South Korea. ²⁶Tel Aviv University, Tel Aviv, Israel. ²⁷University of Regina, Regina, Canada. ²⁸University of South Carolina, Columbia, SC, USA. ²⁹Faculty of Mathematics and Physics, University of Ljubljana, Ljubljana, Slovenia. ³⁰Jožef Stefan Institute, Ljubljana, Slovenia. ³¹Institut de Physique Nucleaire, Orsay, France. ³²Oak Ridge National Laboratory, Oak Ridge, TN, USA. ³³Norfolk State University, Norfolk, VA, USA. ³⁴Yerevan Physics Institute, Yerevan, Armenia. ³⁵Xavier University of Louisiana, New Orleans, LA, USA. ³⁶Chinese Academy of Sciences, Beijing, China. ³⁷Deceased: P. Solvignon-Slifer. ✉e-mail: karl.slifer@unh.edu

Methods

The polarized continuous-wave electron beam was created by stimulating photoemission from a strained GaAs cathode using circularly polarized light. The polarization was flipped at 960 Hz in a pseudo-random fashion. The helicity sequence was a quartet pattern of (+--+), or (----) to minimize linear background effects²⁵. An insertable half-wave plate controlled the overall sign of beam polarization and was flipped throughout the experiment to suppress helicity-dependent systematic effects. The beam polarization was measured using a Møller polarimeter. The average polarization was $84.0 \pm 1.5\%$ (refs. ^{43,44}).

The beam current was kept well below 100 nA; this current limit and a raster system designed to spread the beam spot out to a circle with a diameter of 2 cm were used to minimize target depolarization. New beam position monitors and readout electronics were designed for the experiment to deal with the lower beam current, spiral raster pattern and chicane magnets installed to transport the beam through the large transverse target field⁴⁵. This equipment achieved uncertainties of 1–2 mm and 1–2 mrad in the beam position and beam angle, respectively⁴⁶.

Polarized protons were created by means of dynamic nuclear polarization⁴⁷ of solid ammonia target beads, kept at a temperature of about 1 K in a ⁴He evaporation refrigerator. In dynamic nuclear polarization, polarization enhancement is achieved via microwave-stimulated transitions. Polarization is measured by a nuclear magnetic resonance system, a high-precision resistance–inductance–capacitance circuit capable of detecting photons emitted or absorbed by proton spin flips as a change in the circuit's inductance. A superconducting magnet run at 5.0 and 2.5 T provided the necessary field strengths for the dynamic nuclear polarization process, and the magnet system was rotatable for obtaining parallel and transverse polarization states. The average target polarizations were 70% and 15% for the 5.0 and 2.5 T configurations, respectively⁴⁸.

The scattered electrons were detected by the Hall A high-resolution spectrometers⁴⁹. A room-temperature septum magnet was placed in front of the entrance to each spectrometer and decreased the minimum accepted scattering angle from 12.5° to 6.0°. Drift chambers tracked the electron trajectories and a pair of segmented plastic scintillators formed the data acquisition trigger. Particle identification was provided by a gas Cherenkov detector and a two-layer electromagnetic calorimeter. The efficient organization of readout electronics reduced the processing time and increased the achievable trigger rate to 6 kHz with <20% deadtime.

The polarized cross-section differences used to form the structure functions were calculated from the product of experimental asymmetries ($A_{\parallel,\perp}^{\text{exp}}$) and unpolarized cross sections (σ_0^{exp}) as

$$\Delta\sigma_{\parallel,\perp}^{\text{physics}} = \Delta\sigma_{\parallel,\perp}^{\text{exp}} - \Delta\sigma_{\parallel,\perp}^{\text{tail}} + \delta(\Delta\sigma_{\parallel,\perp}^{\text{RC}}), \quad (8)$$

where $\Delta\sigma_{\parallel,\perp}^{\text{exp}} = 2\sigma_0 A_{\parallel,\perp}$ and radiative correction terms $\Delta\sigma_{\parallel,\perp}^{\text{tail}}$ and $\delta(\Delta\sigma_{\parallel,\perp}^{\text{RC}})$ represent the polarized elastic-tail subtraction and polarized inelastic radiative corrections, respectively. This physics polarized cross-section difference can be approximated as the Born cross section, as the higher-order effects not included in the radiative corrections are heavily suppressed.

The asymmetries were formed according to

$$A^{\text{exp}} = \frac{1}{f \times P_t \times P_b} \left(\frac{Y_+ - Y_-}{Y_+ + Y_-} \right), \quad (9)$$

where $Y_{\pm} = \frac{N_{\pm}}{LT+Q}$ is the LT- and Q-corrected counts (N) for each electron helicity state. The target and beam polarization is accounted for in P_t and P_b , respectively. The dilution factor f corrects for contributions from an unpolarized background. It was determined from the ratio of the experimental scattering data collected on the ammonia target cell,

empty target cell, liquid ⁴He and thin ¹²C disk. The carbon data were used to check and scale the Bosted–Fersch empirical fit⁵⁰. This fit was then used to model the nitrogen background contribution. For this experiment, the dilution factor was usually around 0.15, with some structure varying along W .

At the transverse kinematic settings, an additional correction factor was applied to the asymmetries to account for the out-of-plane angle between the polarization and scattering planes. The correction was applied as $1/\cos(\theta_{\text{OoP}})$. The combination of chicane magnets and target magnetic field caused the asymmetries to acquire a large out-of-plane term. Determined from the beam position monitor and scattered electron reconstruction, the angle ranged from $\theta_{\text{OoP}} = 25^\circ$ – 65° (5.0 T) and $\theta_{\text{OoP}} = 1^\circ$ – 20° (2.5 T).

Data availability

The primary experimental data involved in the findings of this analysis are available in the tables and source data files of this Article, with additional data available on request from K.S. (karl.slifer@unh.edu), D.R. (david.ruth@unh.edu) and J.P.C. (jpchen@jlab.org). Source data are provided with this paper.

Code availability

All the computer codes that support this analysis are available on request from K.S. (karl.slifer@unh.edu), D.R. (david.ruth@unh.edu) and J.P.C. (jpchen@jlab.org).

References

- E08-027 Møller Measurement (accessed 8 September 2015); <http://hallaweb.jlab.org/equipment/moller/e08-027.html>
- Results of Raw Møller Measurement (accessed 8 September 2015); http://hallaweb.jlab.org/equipment/moller/2012_raw_results_archive.html
- Musson, J. *Functional Description of Algorithms Used in Digital Receivers*. Technical Note, Jefferson Lab (2014).
- Zhu, P. et al. Beam position reconstruction for the g2p experiment in Hall A at Jefferson Lab. *Nucl. Instrum. Meth. A* **808**, 1–10 (2016).
- Crabb, D. G. & Meyer, W. Solid polarized targets for nuclear and particle physics experiments. *Annu. Rev. Nucl. Part. Sci.* **47**, 67–109 (1997).
- Pierce, J. et al. Dynamically polarized target for the g_2^p and g_2^n experiments at Jefferson Lab. *Phys. Part. Nucl.* **45**, 303–304 (2014).
- Alcorn, J. et al. Basic instrumentation for Hall A at Jefferson Lab. *Nucl. Instrum. Meth. A* **522**, 294–346 (2004).
- Bosted, P. E. et al. Ratios of ¹⁵N/¹²C and ⁴He/¹²C inclusive electroproduction cross sections in the nucleon resonance region. *Phys. Rev. C* **78**, 015202 (2008).

Acknowledgements

We would like to thank the Hall A technical staff, polarized target group, and the accelerator operators for their efforts and dedication. We would also like to thank J. M. Alarcón, V. Bernard, P. Bosted, E. Christy, A. Deur, E. Epelbaum, F. Hagelstein, H. Krebs, S. Kuhn, V. Lensky, U.-G. Meißner and V. Pascalutsa for their very helpful discussion and suggestions on this publication. This work was supported by the Department of Energy (DOE) under grants DE-FG02-88ER40410 (funding the University of New Hampshire Nuclear Physics group, received by K.S.), DE-FG02-96ER40950 (funding the University of Virginia Polarized Target Group, received by D.D.) and DE-AC02-06CH11357 (funding the Argonne National Lab group, received by P.R.). The Southeastern Universities Research Association operates the Thomas Jefferson National Accelerator Facility for the DOE under contract DE-AC05-06OR23177.

Author contributions

All the authors were involved in the collection of data, design and commissioning of the experimental equipment, or the processing and analysis of the data. The following authors contributed especially to the main analysis and writing of this Article: D.R., J.P.C., K.S. and R.Z.

Competing interests

The authors declare no competing interests.

Additional information

Extended data is available for this paper at <https://doi.org/10.1038/s41567-022-01781-y>.

Supplementary information The online version contains supplementary material available at <https://doi.org/10.1038/s41567-022-01781-y>.

Correspondence and requests for materials should be addressed to K. Slifer.

Peer review information *Nature Physics* thanks Eva-Maria Kabuß, Salvatore Fazio and the other, anonymous, reviewer(s) for their contribution to the peer review of this work.

Reprints and permissions information is available at www.nature.com/reprints.

Q^2 (GeV ²)	0.021	0.045 [†]	0.045	0.086	0.130
$d\Omega dE'$	10	10	10	10	10
f	7	4	8	7	8
$P_b P_t$	5	5	5	5	5
$\Delta\sigma^{\text{RC}}$	3	3	3	3	3
$\Delta\sigma^{\text{tail}}$	3	2	3	3	3
g_1/g_2 input	2	2	1	1	1
Total	14	13	14	14	14

Extended Data Fig. 1 | Measured spin structure function systematic uncertainties. The results are given in %. Systematic uncertainties arise from the target dilution factor f , from beam and target polarizations P_b and P_t , radiative corrections $\Delta\sigma^{\text{RC}}$ and $\Delta\sigma^{\text{tail}}$, the g_1/g_2 inputs into eq. (8), and $d\Omega dE'$, the error on the unpolarized cross section model. Systematic contributions from the out of

plane polarization angle θ_{OoP} and the adjustment of the structure functions to constant Q^2 were evaluated and found to contribute $< 1\%$ to the total systematic error. Reported values are typical of values around the $\Delta(1,232)$ resonance. The columns indicate the systematic associated with each individual Q^2 kinematic setting, as indicated in the first row. [†]Longitudinal kinematic setting.